INORGANIC CHEMISTRY FRONTIERS

RESEARCH ARTICLE

View Article Online
View Journal | View Issue

Cite this: *Inorg. Chem. Front.*, 2024, **11**, 5233

Inorganic Cu_2ZnSnS_4 hole transport layer for perovskite light-emitting diodes†

Lunyao Pan,[a] Wen Li,*[a] Xiankan Zeng,[a] Maolin Mu,[a] Qungui Wang,[b] Yongjian Chen,[a] Chenglong Li,[a] Shiyu Yang,[a] Linzhu Dai,[c] Li Tao[d] and Weiqing Yang *[a,e]

Inorganic Cu_2ZnSnS_4 (CZTS) has garnered significant attention in the field of solar cells owing to its high hole mobility, suitable optical bandgap, cost-effective and earth-abundant elemental constituents. In particular, the deeper highest occupied molecular orbital (HOMO) of CZTS makes it an alternative for the traditional organic hole transport layer (HTL) material poly(3,4-ethyllenedioxythiophene):poly(styrenesulfonate) (PEDOT:PSS), which can suppress acidic interface and hygroscopic problem in perovskite light-emitting diodes (PeLEDs). Herein, we demonstrate CZTS as a novel inorganic HTL for green $FAPbBr_3$ PeLEDs, achieving a peak external quantum efficiency (EQE) of 7.59% and a maximum luminance of 27 000 cd m^{-2} (emitting at 529 nm). The fluorescence properties of the perovskite films and interfacial behaviors of CZTS/$FAPbBr_3$ were investigated through surface state regulation of CZTS HTL. High hole mobility (0–30 cm^2 V^{-1} s^{-1}) of CZTS HTL and low hole injection barrier (~0.13 eV) between CZTS and perovskite endow the CZTS-based PeLEDs with enhanced hole transport capability and suppressed interfacial carrier accumulation. In addition, an attractive cost-effectiveness advantage of about $0.24 per g synthesizing CZTS makes it a promising competitor to mainstream organic HTL materials such as PEDOT:PSS (~$1.3 per g). An in-depth understanding of this novel CZTS HTL makes an essential step forward for the commercialization of PeLEDs.

Received 13th May 2024,
Accepted 26th June 2024

DOI: 10.1039/d4qi01186d

rsc.li/frontiers-inorganic

1. Introduction

In recent years, the research community has made remarkable achievements and quickly rocketed the external quantum efficiency (EQE) of perovskite light-emitting diodes (PeLEDs) to over 20%.[1–6] Nevertheless, the underlying hole transport layer (HTL) in PeLEDs always suffers from confined intrinsic stability, low hole mobility and high injection barrier, substantially creating extra nonradiative losses of carriers at the HTL/perovskite interface. For instance, poly(3,4-ethyllenedioxythiophene):poly(styrenesulfonate) (PEDOT:PSS), as one of the mainstream HTL materials, is characterised by high hydrophilicity, conductivity and transparency.[7] However, there are still several inherent limitations in PEDOT:PSS, including a relatively shallow highest occupied molecular orbital (HOMO) energy level (−5.3 eV), which results in a large energy offset with the valence band maximum (VBM) of the perovskite layer, the acidic and hygroscopic nature leading to severe buried interface deterioration of perovskite films and poor long-term stability of PeLEDs, high product costs (~$1.3 per g) and large batch-to-batch variation severely degrading the cost-benefit ratio of device manufacturing.[8–10] Consequently, the development of novel, low-cost, efficient and stable HTL materials is essential for the resolution of these intractable issues to achieve high-performance PeLEDs.

Compared with organic transport materials, inorganic HTL materials are advantageous in terms of lower production cost, higher environmental stability and facile synthesis, collectively demonstrating the adaptability to the trend of large-scale commercial production of PeLEDs.[11] A few inorganic HTL materials have been incorporated into PeLEDs, including $Cs_{0.32}WO_3$, CuSCN, NiO_x and $Ni_{0.9}Mg_{0.1}O_x$, which afford comparable luminance and EQE.[12–16] However, there is still a shortage of P-type inorganic hole transport materials with both high mobility and deep HOMO energy levels to effectively match those mainstream electron transport layers with high electron mobility. Fortunately, the inorganic P-type semiconductor material Cu_2ZnSnS_4 (CZTS), commonly known as a

[a]Key Laboratory of Advanced Technologies of Materials (Ministry of Education), School of Materials Science and Engineering, Southwest Jiaotong University, Chengdu 610031, PR China. E-mail: wqyang@swjtu.edu.cn, liwen3337@swjtu.edu.cn
[b]College of Physics, Sichuan University, Chengdu 610065, PR China
[c]School of Chemistry and Chemical Engineering, Southwest University, Chongqing 400715, PR China
[d]School of Optoelectronic Engineering, Chengdu University of Information Technology, Chengdu 610225, PR China
[e]Research Institute of Frontier Science, Southwest Jiaotong University, Chengdu 610031, PR China

† Electronic supplementary information (ESI) available. See DOI: https://doi.org/10.1039/d4qi01186d

light absorber material, shows great potential to act as a promising HTL material for its high hole mobility (0–30 $cm^2 V^{-1} s^{-1}$) and deep HOMO energy level (−5.57 eV).[17–20] Besides, remarkably excellent chemical stability, non-toxic nature, high earth crust abundance and low cost (~$0.24 per g) broaden its potential for commercial application in HTL materials.[4–6,18,21] As a high-performance active layer in solar cells, CZTS with good charge carrier transport capacity is easy to generate intriguing and heuristic interfacial carrier behavior when applied as HTL in PeLEDs.[19,22] Thus, it is of great significance to investigate the impact of CZTS HTL on the crystallographic quality of perovskite films and the behavior of interfacial carriers in CZTS-based PeLEDs.

Herein, we employed CZTS as a novel inorganic HTL in $FAPbBr_3$ PeLEDs, which reached a peak EQE of 7.59% and exhibited a pure green luminescence at 529 nm with a maximum luminance of 27 000 cd m^{-2}. In addition, we reveal the relationship of carrier transport and recombination at the CZTS/$FAPbBr_3$ interface with surface state regulation of CZTS HTL. Owing to the deep HOMO energy level and high hole mobility, an appropriate energy offset of 0.13 eV for the CZTS/$FAPbBr_3$ interface dramatically enhanced hole injection capacity and reduced interfacial carrier accumulation in PeLEDs. This study affords a cost-effective inorganic HTL material and highlights the significant potential of inorganic CZTS HTL in future commercial applications of PeLEDs.

2. Experimental section

2.1. Materials

Lead bromide ($PbBr_2$, 99%), copper sulphate ($CuSO_4·5H_2O$), zinc sulphate ($ZnSO_4·7H_2O$), stannous sulfate ($SnSO_4$), sulphur powder, and isopropyl alcohol ($(CH_3)_2CHOH$) were obtained from Shanghai Macklin Co, Ltd. Keshi provided ethanol, toluene (99.9%), octane (98%) and *N*,*N*-dimethylformamide (DMF, 98%). Additionally, molybdenum trioxide (MoO_3, 99.95%), oleylamine (OLA, 90%), oleic acid (OA, 90%) and LiF were sourced from Shanghai Aladdin Industrial Corporation Co., Ltd. Xi'an Polymer Light Technology Corp supplied formamidine bromide (FABr), 2,2′,2″-(1,3,5-benzinetriyl)-tris(1-phenyl-1*H*-benzimidazole) (TPBi, 99.9%) and PEDOT:PSS (Clevios Al 4083). Lastly, Guangdong Poly Optoelectronics Co. Ltd supplied ZnMgO. No further purifications of any materials were required before use.

2.2. Preparation of $FAPbBr_3$ QDs

The synthesis of $FAPbBr_3$ QDs was carried out using a modified method based on the literature. The $FAPbBr_3$ precursor (150 μL), prepared by dissolving $PbBr_2$ and FABr in DMF with a molar ratio of 1 : 2.2 and Pb^{2+} concentration at 0.2 M, was injected into a vial containing a crystallization-inducing solution composed of 5 mL of toluene, 2 mL of 1-butanol, 500 μL of oleic acid, and 30 μL of *n*-diacylamine. The solution was vigorously stirred for 10 minutes after the injection, following which it was centrifuged at 13 000 rpm for 5 minutes and the supernatant was discarded. The precipitate was redispersed in 1 mL of *n*-hexane and then centrifuged at 2000 rpm for 2 minutes. The resulting supernatant was filtered through a 0.22 μm PTFE filter to collect $FAPbBr_3$ QDs. Prior to the injection of the precursor, the crystallization-inducing solution was precooled to 8–10 °C.

2.3. Preparation of CZTS ($W_0/W_1/W_2/W_5$) films

The colloidal CZTS nanocrystals were synthesized using the hot injection method. A mixture of 0.15 M copper sulphate ($CuSO_4·5H_2O$), 0.075 M zinc sulphate ($ZnSO_4·7H_2O$), 0.075 M stannous sulphate ($SnSO_4$), and 10 mL of oleylamine (OLA) was prepared in a three-neck flask at room temperature. The resulting solution was stirred constantly and heated to 130 °C for 40 minutes. Then, the reaction temperature was raised to 240 °C before rapidly injecting 5 mL of our previously prepared sulfur precursor solution (3 M) into the preheated Cu–Zn–Sn–OLA complex solution. After half an hour the reaction was complete. W_0, W_1, W_2 and W_5 inks were purified once, twice, three times and five times respectively, $W_0/W_1/W_2/W_5$ films were obtained by spinning $W_0/W_1/W_2/W_5$ inks on the ITO substrate.

2.4. Device fabrication

$FAPbBr_3$ QDs were spin-coated at 1000 rpm for 60 seconds on the $W_0/W_1/W_2$ films and then quickly transferred into a high-vacuum evaporator without annealing. Afterward, in a low-vacuum environment of 8×10^{-5} Pa, a sequential deposition of 50 nm TPBi, 1 nm of LiF, and 80 nm of Al was carried out. The hole-only device was fabricated by sequentially depositing 3 nm of MoO_3 and 80 nm of Ag onto the perovskite film. The electron-only device was fabricated by replacing the CZTS ($W_0/W_1/W_2$) with the ZnMgO film. The ZnMgO film was prepared by spin-coating ZnMgO (16 mg mL^{-1} in ethanol) at 4000 rpm for 40 seconds on the N_2-plasma-treated ITO and annealed at 120 °C for 10 minutes.

2.5. Characterization

The crystalline structure and quality of the CZTS nanocrystal films were investigated by X-ray diffraction (XRD; X'Pert ProX-ray diffractometer) employing a Cu Kα (λ = 1.5418 Å) and Raman spectroscopy (Renishaw) using an Argon-ion laser (wavelength of 514.5 nm) at room temperature. Raman spectra were acquired at a constant incident laser power of 2.5 mW. A JEOL JSM-7800 Prime scanning electron microscopy (SEM) with an accelerating voltage of 5 kV and atomic force microscopy (AFM, Bruker NanoScope V), with a peak force tapping mode using silicon tips (TESP, Veeco), were used to characterize the morphologies of the films. The UV absorption spectra were obtained using the UV-2500 (Shimadzu Corporation). The PL spectra, TRPL spectra, and temperature-dependent photoluminescence spectra were investigated using an FLS980 (Edinburgh Instruments) spectrometer with a 450 W Xenon lamp. The room-temperature absolute PLQYs of the films were measured on an Edinburgh-FLS 980 spectrometer using an integrating sphere. Fourier transform infrared (FTIR)

spectroscopy patterns were obtained to determine the types and changes of functional groups in materials using a TENSOR II spectrometer (Bruker) with a spectral resolution of 4 cm^{-1} at a scanning frequency of 1 spectra min^{-1}. X-ray photoelectron spectroscopy (XPS) analysis was performed on a Thermo Scientific ESCALAB 250 Xi instrument. UV photoelectron spectroscopy (UPS) measurements were performed at room temperature using the He-discharge lamp (He I line at 21.2 eV) as the excitation source in normal emission with a resolution of 0.06 eV in the ESCALAB 220iXL spectrophotometer. The characterization of hole-only and electron-only devices and low- (f = 5 K) and high-frequency (f = 100 K) capacitance-voltage curves of PeLEDs was performed using the Keithley 4200 device. The Keithley 2400 source meter combined with a QE-Pro spectrometer (Ocean Optics), was employed to characterize the performances of PeLEDs in the glove box. The intensity of electroluminescence was measured using a FOIS-1 integration sphere.

3. Results and discussion

Generally, inorganic compounds serve as hole transport materials in PeLEDs, and their carrier transport performance is significantly influenced by the abundant surface ligands (states).[23–25] Thus, the rational regulation of the surface states of CZTS is a fundamental prerequisite for the first application in PeLEDs as an efficient HTL material. CZTS nanocrystal synthesised by the hot injection method is typically capped with plentiful long-chain oleylamine (OLA) ligands, and their surface states can be effectively regulated through the purification process.[21,26] Fig. 1a illustrates the preparation process of the three different CZTS nanocrystal films with varying washing times (W_0, W_1 and W_2), where toluene and isopropyl alcohol were employed to precisely control the quantity of OLA ligands, thereby effectively modulating the surface states of CZTS. The Tauc's plots demonstrate that the band gap of CZTS films is barely affected by washing times (Fig. S1†).[27,28] Additionally, The HOMO energy level of the three CZTS (−5.57 eV) was determined through ultraviolet photoelectron spectroscopy (UPS), which aligns well with the VBM of $FAPbBr_3$ films (−5.7 eV) and facilitates hole transport at the CZTS/$FAPbBr_3$ interface (Fig. S2†).[29,30] The distinct peaks of X-ray diffraction (XRD) patterns at 28.48°, 32.90°, 47.43° and 56.25° corresponding to (112), (103), (220), and (312) planes, respectively, of the kesterite CZTS phase are shown in Fig. S3,† demonstrating the successful synthesis of pure-phase CZTS.[31] Moreover, Raman spectra exhibit two prominent peaks at 287 cm^{-1} and 337 cm^{-1}, unequivocally confirming the formation of pure quaternary CZTS rather than binary or ternary impurities (Fig. 1b).[32] The consistency observed in both XRD and Raman spectra suggests that the surface state regulation does not affect the crystal structure or orientation of the CZTS films. Furthermore, transmission electron microscopy (TEM) analysis demonstrates uniform dispersion of CZTS nanocrystal films within the toluene solvent with an average particle size of approximately about 6.7 nm (W_0), 6.4 nm (W_1) and 6.9 nm (W_2 sample) (Fig. S4†).[33] The excellent crystallinity and dispersibility of CZTS lay the solid foundation for the application of high-performance HTL in PeLEDs.

X-ray photoelectron spectroscopy (XPS) was performed to confirm the ligand modifications on the surface of the $W_0/W_1/W_2$ films. As shown in Fig. S5,† the carefully calibrated N 1s peaks of $W_0/W_1/W_2$ samples were consistently distributed between 399–402 eV. Additionally, all samples exhibited a characteristic C-NH_2 peak at 400.86 eV, indicating attachment of the OLA ligands on the surface of CZTS films with different washing times.[34] The Fourier-transform infrared spectroscopy (FTIR) patterns of CZTS nanocrystal films are dominated by vibrational modes of bound ligand molecules (Fig. 1c). A noticeable decrease in the intensity of the signal peaks corresponding to C–H stretching vibration (2853 cm^{-1} and 2923 cm^{-1}) and NH_2 bending vibration (1620 cm^{-1}) of the OLA ligands was observed when the CZTS nanocrystal films were purified twice, which suggests a large number of ligands are shed from the CZTS nanocrystals in the purification process and contributes to the surface states differentiation of CZTS.[35,36] Furthermore, the transmittance of the transport layer significantly impacts the efficiency of the photon extraction in PeLEDs. Fig. S6† demonstrates that the transmittance of CZTS films exceeds 90%, and this superior light output characteristic was maintained at a thickness of 120 nm, which means that CZTS has great potential as a novel HTL (Fig. S7†). The SEM images and EDS results shown in Fig. S8,† indicated that Cu, Zn, Sn and S components are uniformly distributed in CZTS films and all three samples are compact and pinhole-free, demonstrating that the varying purification times will not significantly change the morphology of the CZTS nanocrystal films.[33] Parallelly to the atomic force microscope (AFM) images of these three samples in Fig. 1d, the W_0 film without purification displays a low surface roughness with root mean square (RMS) of 5.63 nm, while the roughness of the W_2 film is increased two times than that of the initial W_0 film. Therefore, the surface state regulation method is feasible to optimize the quality of CZTS HTL, which is critical for the charge transport in PeLEDs.

The underlying CZTS nanocrystal films determine the quality of the perovskite (PVK) emission layer (EML).[37–39] The photoluminescence (PL) spectra of $FAPbBr_3$ quantum dots (QDs) on the $W_0/W_1/W_2$ films in Fig. 2a exhibit a homogeneous emission at 526 nm and a distinguishing attenuation of peak intensity. In particular, the CZTS(W_0)/$FAPbBr_3$ film shows the best luminescence properties and longest lifetime (τ_{ave} = 17.76 ns, PLQY = 66.37%) compared to the CZTS(W_1)/$FAPbBr_3$ film (τ_{ave} = 15.04 ns, PLQY = 45.48%) and CZTS(W_2)/$FAPbBr_3$ film (τ_{ave} = 11.23 ns, PLQY = 30.42%) (Fig. 2b and c). The radiation/non-radiation recombination rate (k_r, k_{nr}) was further calculated using formulas (1) and (2) and the obtained parameters are summarized in Table S1 (ESI†). The k_r of $W_0/W_1/W_2$ decreases sequentially while the k_{nr} increases consistently, certifying more OLA ligand retention and relatively flat CZTS film is conducive to maintaining the luminescence pro-

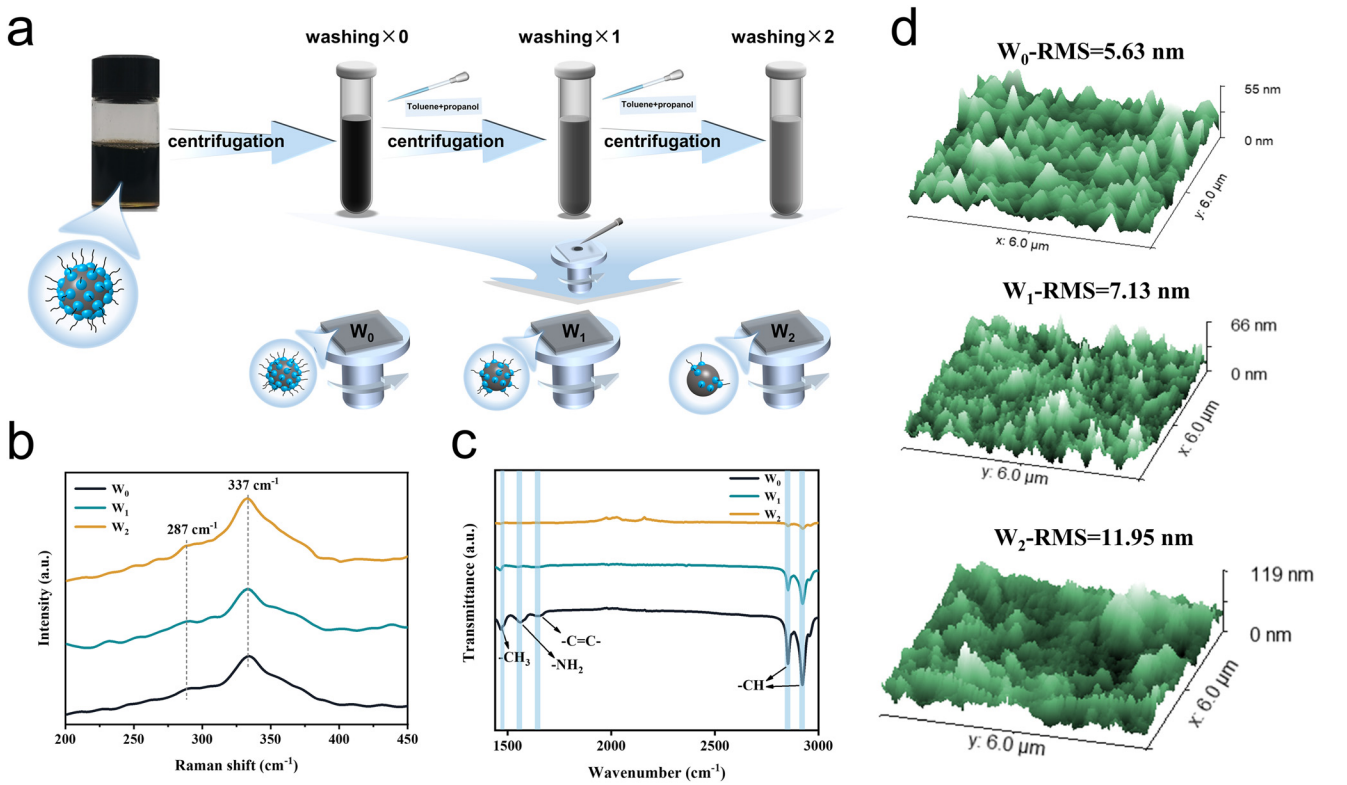

Fig. 1 Characteristics of $W_0/W_1/W_2$ films. (a) Synthetic schematic, (b) Raman spectra, (c) FTIR spectra, and (d) three-dimensional topographic AFM characterization of $W_0/W_1/W_2$ films.

perties of the EML. The CZTS(W_5)/$FAPbBr_3$ film with further reduced OLA ligand retention shows a sharp drop of PLQY (15.28%) (Fig. S9†), which intuitively illustrates the decrease of ligands will expose a number of undesired defects on the CZTS/$FAPbBr_3$ interface and severely deteriorates the optical performance. Furthermore, it is also noteworthy that the transmittance of both $W_0/W_1/W_2$ films exceeds 90%, which indicates that the change of PLQY is independent of the photocoupling efficiency (Fig. S6†).

$$\frac{1}{\tau_{ave}} = k_r + k_{nr} \quad (1)$$

$$PLQY = \frac{k_r}{k_r + k_{nr}} \quad (2)$$

It is worth mentioning that the bottom transport layer enables the easy dissociation of light-activated excitons in the perovskite layer, leading to relatively low PLQY and average PL lifetime. Temperature-dependent PL spectra provide insights into the non-radiative relaxation processes and exciton–phonon coupling behavior, revealing the influence of the CZTS transport layer on the luminescence properties of EML. The broadening of temperature-dependent PL spectra can explain phonon scattering in the perovskite films. The FWHM curve extracted from Fig. 2d–f was fitted, and the experimental data are in good consistency with the optimal fitting curve (R^2 > 0.990, Fig. 2g), the obtained parameters are summarized in Table S1.† The variation of FWHM broadening with temperature is described by formula (3):[37,40,41]

$$\Gamma(T) = \Gamma_0 + \Gamma_{AC} + \Gamma_{LO} = \Gamma_{inh} + \gamma_{AC}T + \gamma_{LO}/[e^{E_{LO}/k_B T} - 1] \quad (3)$$

where Γ_0 is an intrinsic inhomogeneous broadening term associated with material composition, size, and shape. Γ_{AC} results from acoustic scattering and Γ_{inh} stems from optical phonon scattering, both contributing to homogeneous PL emission broadening. γ_{AC} and γ_{LO} depict the strengths of exciton–phonon coupling, k_B is the Boltzmann constant and E_{LO} denotes the phonon energy. The contribution of the acoustic phonon scattering to PL broadening can be neglected for all $FAPbBr_3$ QDs, while the primary contribution of PL broadening comes from the optical phonon scattering. Thus, the higher E_{LO} represents better lattice stability of the $FAPbBr_3$ film, while the gradual decrease of E_{LO} indicates that less ligand-coated CZTS destroy the lattice stability of $FAPbBr_3$ QDs. E_B of the $FAPbBr_3$/CZTS film was fitted using the Arrhenius equation (formula (4)):[42–46]

$$I(T) = \frac{I_0}{1 + Ae^{(-E_B/k_B T)}} \quad (4)$$

where I_0 is the PL integral strength at the temperature of T_0, A is the proportional coefficient, and E_B is the exciton binding energy. As shown in Fig. 2h, the E_B of the $FAPbBr_3$/CZTS films

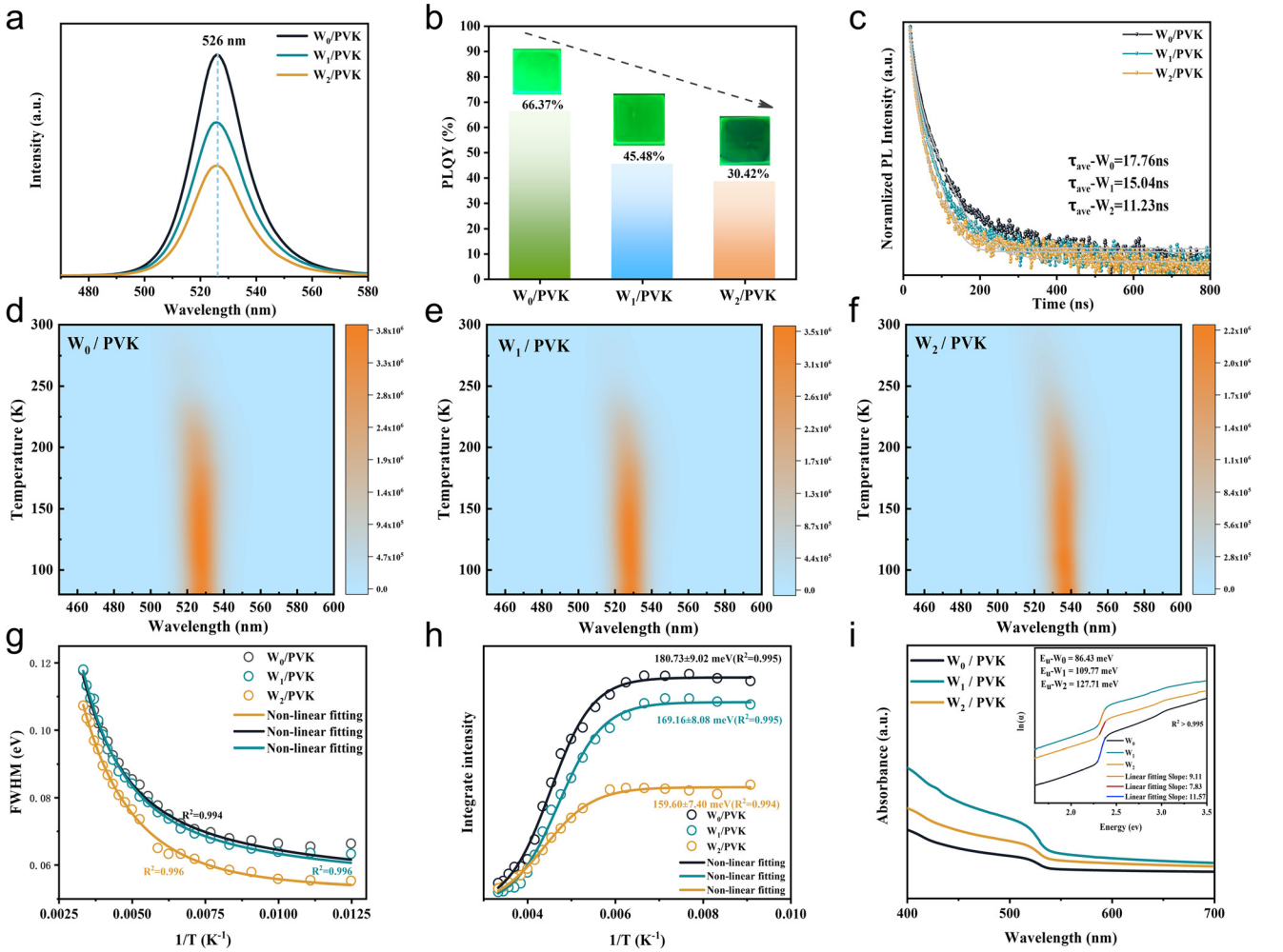

Fig. 2 Photophysical properties of the perovskite films on $W_0/W_1/W_2$ films. (a) PL spectra, (b) PLQY spectra, (c) TRPL spectra, (d, e and f) temperature-dependent PL spectra of the perovskite films on $W_0/W_1/W_2$, (g) FWHM, (h) integrated PL intensity as a function of reciprocal temperature, (i) UV-vis and Urbach energy spectra of the perovskite films on $W_0/W_1/W_2$ films.

decreases from 180.73 meV to 159.60 meV. Higher binding energy indicates a reduction of excitons dissociating into free carriers, suggesting more OLA ligands of the CZTS films can inhibit exciton dissociation and increase radiation recombination in emission films. The interface defects between the CZTS film with fewer ligands and EML increase, and exciton dissociation is easy to occur, which eventually leads to obvious degradation of optical properties.

Urbach tail is the broadening effect of semiconductor band edges related to thermal and inherent structural disorder, quantified by the Urbach energy (E_u).[47,48] The E_u value of CZTS/$FAPbBr_3$ is increased from 86.43 meV to 127.71 meV, as shown in Fig. 2i, indicating that the presence of sufficient ligands of CZTS film can maintain the integrity of the $FAPbBr_3$ lattice. Additionally, the diffraction peaks for the CZTS/$FAPbBr_3$ films exhibit slight shifts to smaller angles, measured at 0.04°, 0.05°, and 0.07° in Fig. S10.†[49–51] This shift implies that Cu^+ (76 pm) or Zn^{2+} (74 pm) with the smaller ionic radius than FA^+ (263 pm) might be partially incorporated into the perovskite lattice in the presence of decreased OLA ligands, resulting in destroyed perovskite QDs and poor photophysical properties of EML.[52] Therefore, the regulation of surface states in CZTS HTL significantly influences the photophysical behavior of perovskite materials.

To investigate the carrier behavior of CZTS-based PeLEDs, we utilized capacitor–voltage (*C–V*) characteristics to evaluate the injection, capture, and recombination behavior in PeLEDs.[53–55] Fig. 3a depicts the low-frequency *C–V* characteristic diagram, segmented into four regions. At lower applied voltages, the similar barrier capacitance of these PeLEDs implies comparable carrier accumulation at the interface prior to injection into the EML (region 2). As the applied voltage surpasses a certain threshold in region 3, the diffusion capacitance reflects the ability of the majority carriers to transport between the transport layer and the EML layer. Notably, the diffusion capacitance (C_3) of W_0-based PeLEDs is 2.83 nF, which markedly surpasses that of the W_1-based PeLEDs (2.46 nF) and W_2-based PeLEDs (2.31 nF), suggesting that the pres-

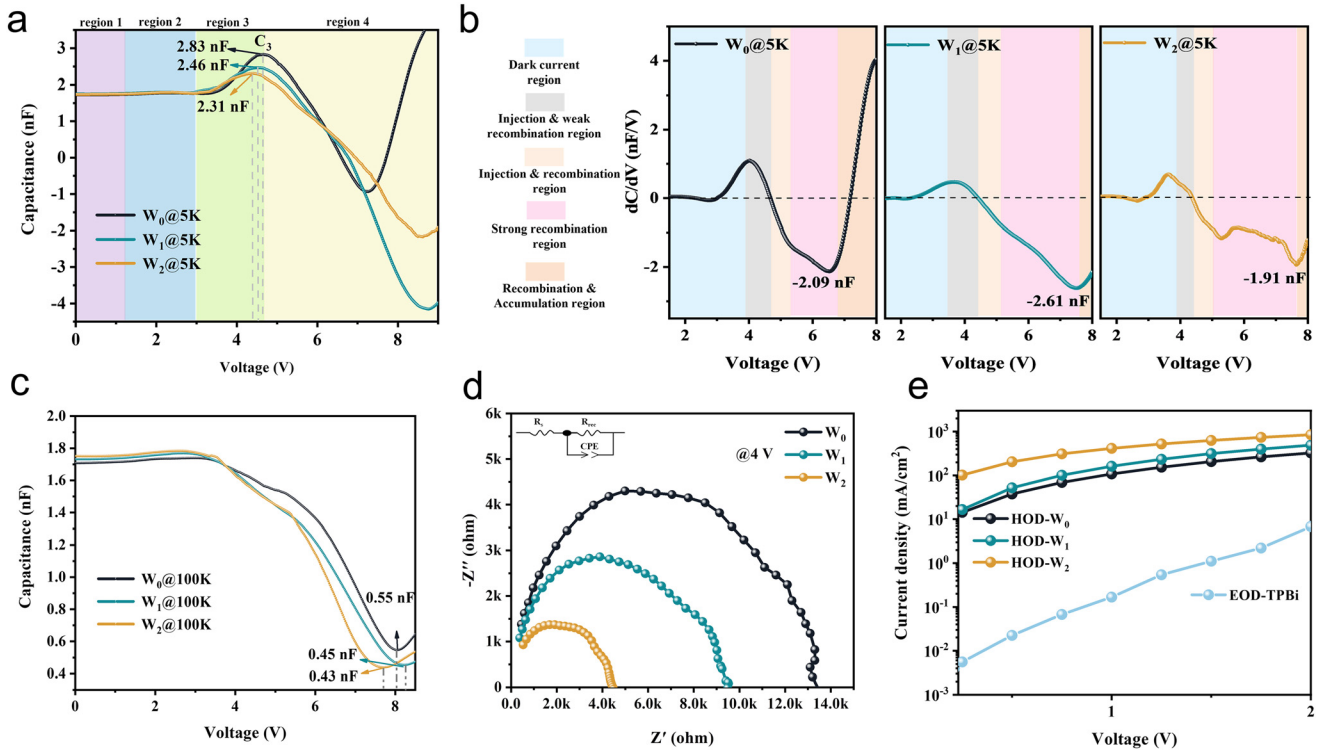

Fig. 3 Carrier behavior in PeLEDs. (a) Low-frequency capacitance–voltage (*C*–*V*) plots (*f* = 5 K), (b) d*C*/d*V*–*V* curves, (c) high-frequency *C*–*V* plots (*f* = 100 K) of CZTS-based PeLEDs. (d) Nyquist plots of impedance spectra and (e) current density–voltage (*J*–*V*) characteristics curves of hole-only device and electron-only devices of CZTS-based PeLEDs. The inset shows the equivalent circuit diagram for fitting.

ence of long-chain OLA ligands on CZTS substantially impedes hole transport between HTL and EML. Furthermore, a decline in region 4 indicates carrier recombination has occurred.[56,57] Particularly, there is a more pronounced drop in capacitance for W_1-based-PeLEDs compared to W_0/W_2-based PeLEDs, indicating intensified carrier radiative recombination in W_1-based PeLEDs. Furthermore, the presence of OLA ligands in W_0-based PeLEDs hampers carrier transport, leading to a reduced number of carriers capable of efficient radiative recombination during voltage increase. As a result, the capacitance prematurely increases after 7 V. Fig. 3b illustrates the differentiation of the three *C*–*V* curves in Fig. 3a, represented by capacitance-voltage derivative (d*C*/d*V*) and categorized into five distinct regions. A negative slope in d*C*/d*V* indicates a strong recombination region. In comparison, W_1-based PeLEDs exhibit a larger negative value in d*C*/d*V* compared to W_0/W_2 based-PeLEDs, suggesting that W_1-based PeLEDs possess stronger recombination ability.

Under high-frequency conditions, trapped carriers are significantly suppressed, thereby our focus was directed toward investigating the relationship between carrier injection and recombination (Fig. 3c). A smaller capacitance at higher voltages indicates enhanced carrier recombination, with W_1-based PeLEDs exhibiting a diminished trend of negative d*C*/d*V* (Fig. S11†), which aligns with the observed intense carrier recombination in W_1-based PeLEDs as evidenced by low-frequency *C*–*V* curves. These findings indicate that an excess of OLA ligands on the CZTS surface impedes interface carrier injection and diffusion, while proper surface states promote carrier recombination.

Electrical impedance spectroscopy (EIS) measurements confirmed the disparity at the interface of PeLEDs.[58–61] CZTS-based PeLEDs devices were subjected to 4 V bias within the frequency range of 0.1 Hz to 1 MHz. As depicted in Fig. 3d, the electron transfer impedance (or resistance) of CZTS/$FAPbBr_3$ was determined by fitting an equivalent circuit diagram derived from the Nyquist curve. Utilizing the illustrated equivalent circuit (Fig. 3d), it is evident that W_0-based PeLEDs exhibit a higher series resistance value (R_s) of 13.5 kΩ compared to W_1-based PeLEDs (9.8 kΩ) and W_2-based PeLEDs (4.3 kΩ). This observation suggests a more efficient carrier transfer from W_2-CZTS HTL to EML, which aligns with the impedance characteristics displayed in Fig. S12† for different batches of CZTS. Furthermore, the single-carrier device measurement in Fig. 3e also demonstrates the inhibitory effect of OLA ligands on the charge transport.

According to the variation of photophysical characteristics and interfacial carrier behavior of CZTS-based PeLEDs, Fig. 4 presents a schematic diagram illustrating the carrier transport and recombination mechanism at the CZTS/$FAPbBr_3$ interface. Owing to the insulating nature, excessive OLA ligands hinder carrier transport at the CZTS/$FAPbBr_3$ interface and increase the series resistance, meanwhile, the large carrier accumulation increases the non-radiative recombination. Conversely, a

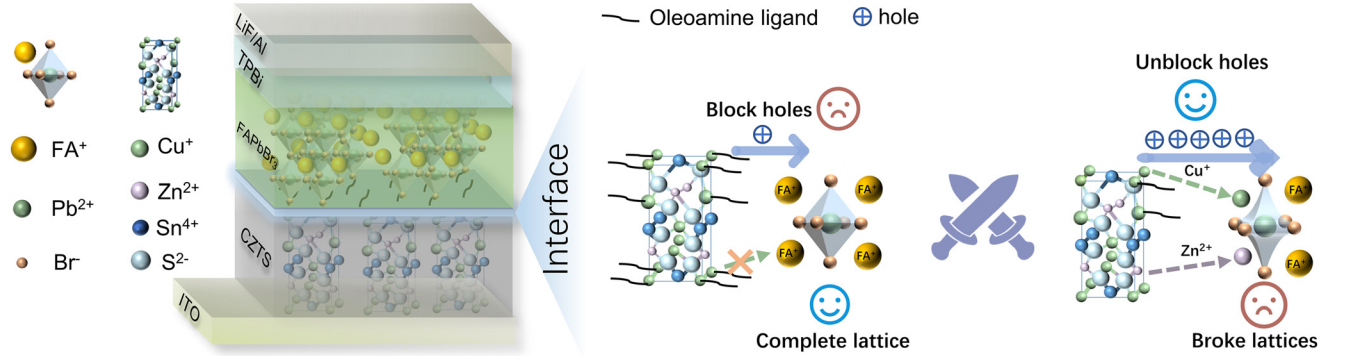

Fig. 4 Schematic diagram of carrier behaviour at CZTS/$FAPbBr_3$ interface.

lack of OLA ligands may permit Cu^+ or Zn^{2+} ions to infiltrate into EML breaking the integrity of the perovskite lattice, which is detrimental to radiative recombination. Satisfyingly, the appropriate ligands on the CZTS (W_1) surface are the best solution to balance the optical property of EML and carrier transport in PeLEDs. Optimal surface state regulation can effectively passivate interface defects and minimize their direct contact with $FAPbBr_3$, thereby stabilizing the perovskite lattice, maintaining the optical properties of $FAPbBr_3$ and facilitating carrier transport/recombination.

To explore the application of the CZTS HTL in PeLEDs, CZTS-based $FAPbBr_3$ PeLEDs devices were fabricated and the schematic structure and energy level diagram are illustrated in Fig. 5a and b. The current density–voltage (J–V) curves depicted in Fig. 5c exhibit an increase in the current density occurring at voltages lower than approximately 4 V, indicating that controlling the surface states of CZTS can effectively suppress leakage current, which aligns with our quality characterization analysis of perovskite films. Samples with a higher concentration of OLA ligand (W_0) exhibit an enhanced carrier

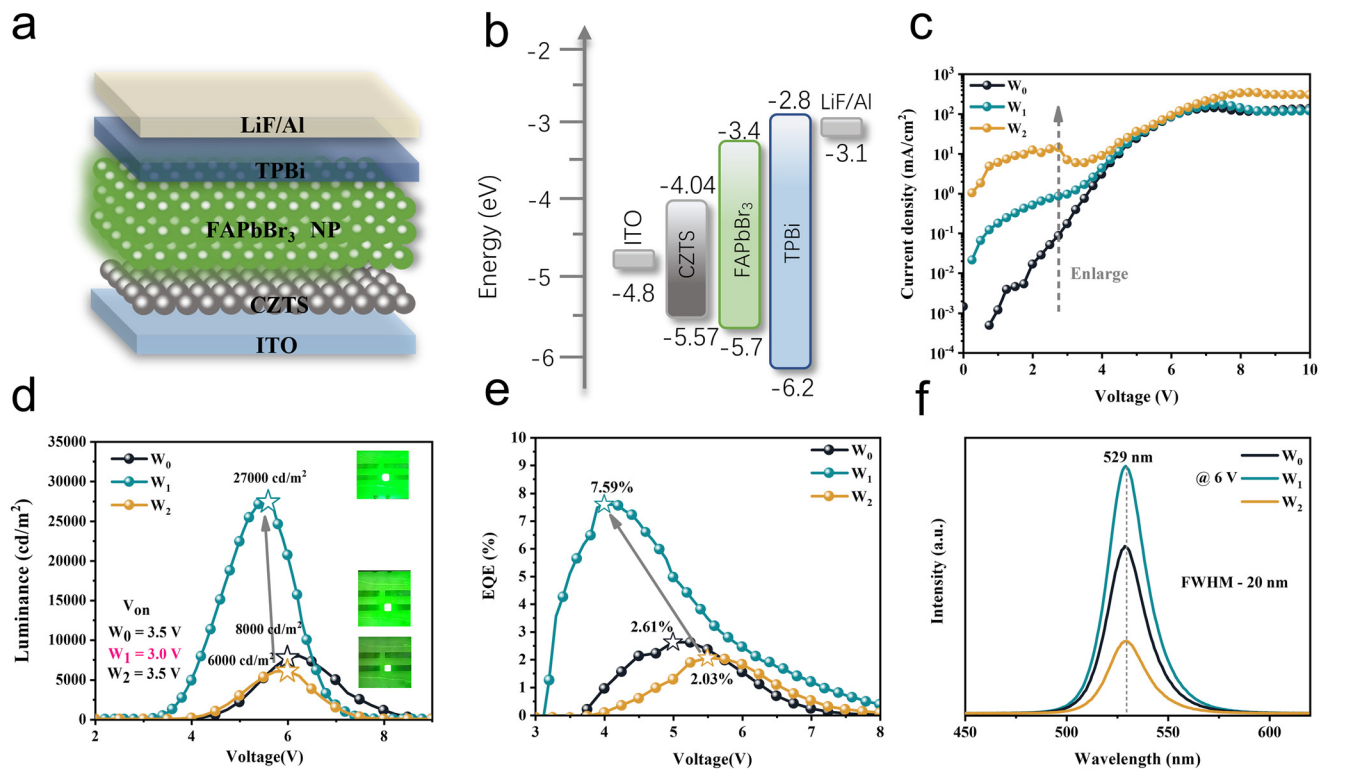

Fig. 5 Device structure and EL performance characteristics of $W_0/W_1/W_2$-based green PeLEDs. (a) Schematic device structure, (b) schematic energy levels, (c) current density–voltage (J–V) characteristics curves, (d) luminance–voltage characteristics curves (L–V), (e) EQE-voltage curves and (f) normalized EL spectra at 6V driving voltage of $W_0/W_1/W_2$-based PeLEDs.

accumulation (Fig. 3a), leading to increased non-radiative recombination and thus reduced device performance. Meanwhile, when the voltage is beyond 4 V, the accumulated carriers exhibit an augmented conduction current subsequent to conduction, thereby demonstrating a current density similar to W_1.[57,62,63] However, as the OLA ligand content decreases significantly (W_2) or is completely absent (W_5), severe damage occurs to the perovskite lattice with a substantial reduction of device series resistance in EIS analysis. Consequently, it can even resemble conductor-like characteristics leading to breakdown at high voltage (Fig. S14a).[64–66] As observed in Fig. 5d and e, W_0-based PeLEDs demonstrate poor performance with a maximum luminance of 8000 cd m^{-2} and a maximum EQE of 2.61%, while the EQE of W_2 device is only 2.03% with luminance dropping to 6000 cd m^{-2}. Surprisingly, device W_1 achieves a peak EQE of 7.59% along with a high maximum luminance of 27 000 cd m^{-2}. It is noteworthy that W_1-based PeLEDs demonstrate a lower turn-on voltage (V_{on}) than other devices by 0.5 V, which is consistent with a low carrier injection barrier and effective carrier radiation recombination. To ensure data reliability and eliminate testing variability, we extracted the last ten instances of device performance and generated a statistical plot as shown in Fig. S13.† Remarkably, the average V_{on} of the W_1-based PeLEDs was found to be smaller than that of the other two samples (with a reduction ranging from 0 to 0.4 V). We propose that CZTS, being a novel inorganic HTL, abundant in metal ions, may disrupt the perovskite lattice upon direct contact with it, leading to a decrease in the radiation recombination efficiency of the W_2 device. V_{on} signifies the initiation of carrier radiative recombination, while excessive insulating ligands in the W_0-based PeLEDs impede carrier transport efficiency. As a result, the W_1 device has lower V_{on} than other devices in terms of carrier transport and perovskite lattice integrity. For the W_5-based PeLEDs (Fig. S14†), the luminance and peak EQE reach as low as 1350 cd m^{-2} and 0.6%. This substantial fluctuation confirms that effective regulation of the surface states of CZTS HTL is an efficient approach to enhancing device performance. The inset in Fig. 5d displays a regular change in brightness of EL emission, providing visual evidence for this improvement. The EL spectra consistently exhibited emission at 529 nm as the bias increased, while maintaining a narrow full-width half-maximum (FWHM) of 20 nm at 6 V, suggesting that CZTS-based PeLEDs devices have superior spectral stability (Fig. S15† and Fig. 5f). Multiple batches of $FAPbBr_3$ PeLEDs were fabricated, and the histograms of peak EQE obviously depict the reproducibility and overall trend in device performance with varying CZTS HTLs (Fig. S16†); the average EQE of the W_0 device is 2.36%, W_1 device is 7.32% and W_2 device 2.09%. Additionally, the half-life (T_{50}) represents the time required for the luminance to decay from 100 cd m^{-2} to 50 cd m^{-2} under constant voltage in a device. It can be calculated using the formula $L_0{}^nT_{50} = a$, where L_0 denotes the initial luminance, n is the exponential parameter characterizing the device, and a is a constant. In comparison with the PEDOT:PSS-based PeLEDs, CZTS equipment exhibits an increased T_{50} from 15.91 min to 43.48 min, indicating improved device stability that can be attributed to the inherent strong stability of CZTS itself (Fig. S17†). Therefore, CZTS shows great potential as HTM for PeLEDs applications.

4. Conclusions

In summary, we have successfully incorporated CZTS as a novel inorganic HTL with low toxicity, deep HOMO energy level, high hole mobility and cost-effectiveness into PeLEDs for the first time. The undesirable charge accumulation and non-radiative recombination at the CZTS/$FAPbBr_3$ interface are significantly suppressed by selectively optimizing the surface state distribution of CZTS nanocrystals. Thus, a pure green $FAPbBr_3$ PeLED device stably emitting at 529 nm with a peak EQE of 7.59% and a highest luminance of 27 000 cd m^{-2} was fabricated; the stability of the CZTS-based PeLEDs is comparatively higher than that of the PEDOT:PSS device (T_{50} increased from 15.91 min to 43.48 min). This study unveils the previously undiscussed impact of surface state regulation of transport layer materials on the interfacial carrier behavior in PeLEDs, maximizing the application value of CZTS as a novel inorganic HTL material in high-performance PeLEDs. This work paves the way for the development of low-toxicity and cost-effective HTL materials, which could facilitate the large-scale production and future commercialization of PeLEDs and other luminescence applications.

Data availability

The authors confirm that the data supporting the findings of this study are available within the article or its ESI.† Moreover, the data that support the findings of this study are available from the corresponding author, upon reasonable request.

Conflicts of interest

The authors declare that they have no known competing financial interests or personal relationships that could have appeared to influence the work reported in this paper.

Acknowledgements

This work was supported by the National Natural Science Foundation of China (No. 52202188 and 11704050). The authors would like to thank the Analysis and Testing Center of Southwest Jiaotong University for supporting the TEM and XRD measurements.

References

1 Z. Liu, W. Qiu, X. Peng, G. Sun, X. Liu, D. Liu, Z. Li, F. He, C. Shen and Q. Gu, Perovskite light-emitting diodes with EQE exceeding 28% through a synergetic dual-additive strategy for defect passivation and nanostructure regulation, *Adv. Mater.*, 2021, **33**, 2103268.

2 J. Jiang, Z. Chu, Z. Yin, J. Li, Y. Yang, J. Chen, J. Wu, J. You and X. Zhang, Red perovskite light-emitting diodes with efficiency exceeding 25% realized by co-spacer cations, *Adv. Mater.*, 2022, **34**, 2204460.

3 S. Yuan, L. Dai, Y. Sun, F. Auras, Y. H. Zhou, R. Z. An, Y. Liu, C. Ding, C. Cassidy, X. Tang, S. C. Dong, H. B. Kang, K. Chen, X. Liu, Z. F. Ye, Y. Zhao, C. Adachi, L. S. Liao, N. C. Greenham, Y. Qi, S. D. Stranks, L. S. Cui and R. H. Friend, Efficient blue electroluminescence from reduced-dimensional perovskites, *Nat. Photonics*, 2024, **24**, 01382–01386.

4 Y. Jiang, C. Sun, J. Xu, S. Li, M. Cui, X. Fu, Y. Liu, Y. Liu, H. Wan, K. Wei, T. Zhou, W. Zhang, Y. Yang, J. Yang, C. Qin, S. Gao, J. Pan, Y. Liu, S. Hoogland, E. H. Sargent, J. Chen and M. Yuan, Synthesis-on-substrate of quantum dot solids, *Nature*, 2022, **612**, 679–684.

5 K. Lin, J. Xing, L. N. Quan, F. P. G. de Arquer, X. Gong, J. Lu, L. Xie, W. Zhao, D. Zhang, C. Yan, W. Li, X. Liu, Y. Lu, J. Kirman, E. H. Sargent, Q. Xiong and Z. Wei, Perovskite light-emitting diodes with external quantum efficiency exceeding 20 per cent, *Nature*, 2018, **562**, 245–248.

6 S. P. Senanayak, K. Dey, R. Shivanna, W. Li, D. Ghosh, Y. Zhang, B. Roose, S. J. Zelewski, Z. Andaji-Garmaroudi, W. Wood, N. Tiwale, J. L. MacManus-Driscoll, R. H. Friend, S. D. Stranks and H. Sirringhaus, Charge transport in mixed metal halide perovskite semiconductors, *Nat. Mater.*, 2023, **22**, 216–224.

7 H. Yu, L. Chen, S. Liu, L. Zhang, W. Xie and C. S. Lee, Solution-processed self-stratifying layer with controllable dielectric polarization for high-luminance organic light-emitting diodes, *Chem. Mater.*, 2023, **35**, 3484–3493.

8 H. Choi, C. K. Mai, H. B. Kim, J. Jeong, S. Song, G. C. Bazan, J. Y. Kim and A. J. Heeger, Conjugated polyelectrolyte hole transport layer for inverted-type perovskite solar cells, *Nat. Commun.*, 2015, **6**, 7348.

9 B. R. Lee, J. w. Kim, D. Kang, D. W. Lee, S. J. Ko, H. J. Lee, C. L. Lee, J. Y. Kim, H. S. Shin and M. H. Song, Highly efficient polymer light-emitting diodes using graphene oxide as a hole transport layer, *ACS Nano*, 2012, **6**, 2984–2991.

10 J. M. Yun, J. S. Yeo, J. Kim, H. G. Jeong, D. Y. Kim, Y. J. Noh, S. S. Kim, B. C. Ku and S. I. Na, Solution-processable reduced graphene oxide as a novel alternative to PEDOT: PSS hole transport layers for highly efficient and stable polymer solar cells, *Adv. Mater.*, 2011, **23**, 4923–4928.

11 A. G. Ricciardulli, S. Yang, N. B. Kotadiya, G. J. A. H. Wetzelaer, X. Feng and P. W. M. Blom, Improved hole injection into perovskite light-emitting diodes using a black phosphorus interlayer, *Adv. Electron. Mater.*, 2019, **5**, 1800687.

12 R. Chakraborty, H. Bhunia, S. Chatterjee and A. J. Pal, Surface-modification of Cu_2O nanoparticles towards band-optimized hole-injection layers in $CsPbBr_3$ perovskite light-emitting diodes, *J. Solid State Chem.*, 2020, **281**, 121021.

13 S. Q. Sun, J. W. Tai, W. He, Y. J. Yu, Z. Q. Feng, Q. Sun, K. N. Tong, K. Shi, B. C. Liu and M. Zhu, Enhancing light outcoupling efficiency via anisotropic low refractive index electron transporting materials for efficient perovskite light-emitting diodes, *Adv. Mater.*, 2024, 2400421.

14 S. Zhuang, J. He, X. Ma, Y. Zhao, H. Wang and B. Zhang, Fabrication and optimization of hole transport layer NiO for all inorganic perovskite light emitting diodes, *Mater. Sci. Semicond. Process.*, 2020, **109**, 104924.

15 Y. L. Shi, M. P. Zhuo, X. C. Fang, X. Q. Zhou, X. D. Wang, W. F. Chen and L. S. Liao, Efficient all-inorganic perovskite light-emitting diodes with cesium tungsten bronze as a hole-transporting layer, *J. Phys. Chem. Lett.*, 2020, **11**, 7624–7629.

16 M. Michalska, M. A. Surmiak, F. Maasoumi, D. C. Senevirathna, P. Chantler, H. Li, B. Li, T. Zhang, X. Lin and H. Deng, Microfluidic processing of ligand-engineered NiO nanoparticles for low-temperature hole-transporting layers in perovskite solar cells, *Sol. RRL*, 2021, **5**, 2100342.

17 B. R. Bade, S. R. Rondiya, Y. A. Jadhav, M. M. Kamble, S. V. Barma, S. B. Jathar, M. P. Nasane, S. R. Jadkar, A. M. Funde and N. Y. Dzade, Investigations of the structural, optoelectronic and band alignment properties of Cu_2ZnSnS_4 prepared by hot-injection method towards low-cost photovoltaic applications, *J. Alloys Compd.*, 2021, **854**, 157093.

18 T. J. Huang, X. Yin, C. Tang, G. Qi and H. Gong, A low-cost, ligand exchange-free strategy to synthesize large-grained Cu_2ZnSnS_4 thin-films without a fine-grain underlayer from nanocrystals, *J. Mater. Chem. A*, 2015, **3**, 17788–17796.

19 S. W. Shin, S. M. Pawar, C. Y. Park, J. H. Yun, J. H. Moon, J. H. Kim and J. Y. Lee, Studies on Cu_2ZnSnS_4 (CZTS) absorber layer using different stacking orders in precursor thin films, *Sol. Energy Mater. Sol. Cells*, 2011, **95**, 3202–3206.

20 A. Tumbul, F. Aslan, A. Göktaş and I. H. Mutlu, All solution processed superstrate type Cu_2ZnSnS_4 (CZTS) thin film solar cell: effect of absorber layer thickness, *J. Alloys Compd.*, 2019, **781**, 280–288.

21 B. Liu, J. Guo, R. Hao, L. Wang, K. Gu, S. Sun and A. Aierken, Effect of Na doping on the performance and the band alignment of CZTS/CdS thin film solar cell, *Sol. Energy*, 2020, **201**, 219–226.

22 Q. Wang, Y. Chen, C. Yan, X. Zeng, X. Fu, L. Pan, J. Cao, S. Yang, W. Li and X. Chen, Molecularly designing a passivation ETL to suppress EQE roll-off of PeLEDs, *ACS Energy Lett.*, 2023, **8**, 3710–3719.

23 B. Bai, D. Kou, W. Zhou, Z. Zhou and S. Wu, Application of quaternary Cu_2ZnSnS_4 quantum dot-sensitized solar cells

based on the hydrolysis approach, *Green Chem.*, 2015, **17**, 4377–4382.

24 A. Carrete, A. Shavel, X. Fontané, J. Montserrat, J. Fan, M. Ibáñez, E. Saucedo, A. Pérez-Rodríguez and A. Cabot, Antimony-based ligand exchange to promote crystallization in spray-deposited $Cu_2ZnSnSe_4$ solar cells, *J. Am. Chem. Soc.*, 2013, **135**, 15982–15985.

25 L. S. Khanzada, I. Levchuk, Y. Hou, H. Azimi, A. Osvet, R. Ahmad, M. Brandl, P. Herre, M. Distaso and R. Hock, Effective ligand engineering of the Cu_2ZnSnS_4 nanocrystal surface for increasing hole transport efficiency in perovskite solar cells, *Adv. Funct. Mater.*, 2016, **26**, 8300–8306.

26 L. Korala, M. B. Braun, J. M. Kephart, Z. Tregillus and A. L. Prieto, Ligand-exchanged CZTS nanocrystal thin films: does nanocrystal surface passivation effectively improve photovoltaic performance?, *Chem. Mater.*, 2017, **29**, 6621–6629.

27 D. Xia, P. Lei, Y. Zheng and B. Zhou, Synthesis and characterization of Cu_2ZnSnS_4 nanocrystals by hot-injection method, *J. Mater. Sci.: Mater. Electron.*, 2015, **26**, 5426–5432.

28 M. Zhou, Y. Gong, J. Xu, G. Fang, Q. Xu and J. Dong, Colloidal CZTS nanoparticles and films: preparation and characterization, *J. Alloys Compd.*, 2013, **574**, 272–277.

29 Z. O. Elhmaidi, R. Pandiyan, M. Abd-Lefdil, E. Saucedo and M. A. El Khakani, *In situ* tuning of the zinc content of pulsed-laser-deposited CZTS films and its effect on the photoconversion efficiency of p-CZTS/n-Si heterojunction photovoltaic devices, *Appl. Surf. Sci.*, 2020, **507**, 145003.

30 S. Kumar, V. Kumar, V. Mikli, T. Varema, M. Altosaar and M. Grossberg, Study of CZTS nano-powder synthesis by hot injection method by variation of Cu and Zn concentrations, *Energy Procedia*, 2016, **102**, 136–143.

31 J. J. Wang, J. S. Hu, Y. G. Guo and L. J. Wan, Wurtzite $Cu_2ZnSnSe_4$ nanocrystals for high-performance organic–inorganic hybrid photodetectors, *NPG Asia Mater.*, 2012, **4**, e2.

32 H. Zhou, W. C. Hsu, H. S. Duan, B. Bob, W. Yang, T. B. Song, C. J. Hsu and Y. Yang, CZTS nanocrystals: a promising approach for next generation thin film photovoltaics, *Energy Environ. Sci.*, 2013, **6**, 2822–2838.

33 S. K. Verma, R. Verma, Y. Xie, D. Xiong, W. Chen, C. Hu, T. A. Emmanuel, M. Wang and X. Zhao, Heat-up and gram-scale synthesis of Cu-poor CZTS nanocrystals with controllable compositions and shapes, *CrystEngComm*, 2017, **19**, 2013–2020.

34 D. Wilson and M. A. Langell, XPS analysis of oleylamine/oleic acid capped Fe_3O_4 nanoparticles as a function of temperature, *Appl. Surf. Sci.*, 2014, **303**, 6–13.

35 M. Chen, Y. G. Feng, X. Wang, T. C. Li, J. Y. Zhang and D. J. Qian, Silver nanoparticles capped by oleylamine: formation, growth, and self-organization, *Langmuir*, 2007, **23**, 5296–5304.

36 Q. Zhao, H. Li, X. Zhang, S. Yu, S. Wang and G. Sun, Platinum *in situ* catalytic oleylamine combustion removal process for carbon supported platinum nanoparticles, *J. Energy Chem.*, 2020, **41**, 120–125.

37 X. Zeng, C. Yan, Q. Wang, J. Cao, X. Fu, S. Yang, Y. Chen, L. Pan, W. Li and W. Yang, High curvature PEDOT: PSS transport layer toward enhanced perovskite light-emitting diodes, *Small*, 2023, **19**, 2304411.

38 D. Shi, V. Adinolfi, R. Comin, M. Yuan, E. Alarousu, A. Buin, Y. Chen, S. Hoogland, A. Rothenberger and K. Katsiev, Low trap-state density and long carrier diffusion in organolead trihalide perovskite single crystals, *Science*, 2015, **347**, 519–522.

39 Z. Wu, M. Jiang, Z. Liu, A. Jamshaid, L. K. Ono and Y. Qi, Highly efficient perovskite solar cells enabled by multiple ligand passivation, *Adv. Energy Mater.*, 2020, **10**, 1903696.

40 B. Ai, C. Liu, Z. Deng, J. Wang, J. Han and X. Zhao, Low temperature photoluminescence properties of $CsPbBr_3$ quantum dots embedded in glasses, *Phys. Chem. Chem. Phys.*, 2017, **19**, 17349–17355.

41 T. J. Savenije, C. S. Ponseca Jr, L. Kunneman, M. Abdellah, K. Zheng, Y. Tian, Q. Zhu, S. E. Canton, I. G. Scheblykin and T. Pullerits, Thermally activated exciton dissociation and recombination control the carrier dynamics in organometal halide perovskite, *J. Phys. Chem. Lett.*, 2014, **5**, 2189–2194.

42 V. M. Le Corre, E. A. Duijnstee, O. El Tambouli, J. M. Ball, H. J. Snaith, J. Lim and L. J. A. Koster, Revealing charge carrier mobility and defect densities in metal halide perovskites via space-charge-limited current measurements, *ACS Energy Lett.*, 2021, **6**, 1087–1094.

43 Z. Ren, J. Yu, Z. Qin, J. Wang, J. Sun, C. C. S. Chan, S. Ding, K. Wang, R. Chen and K. S. Wong, High-performance blue perovskite light-emitting diodes enabled by efficient energy transfer between coupled quasi-2D perovskite layers, *Adv. Mater.*, 2021, **33**, 2005570.

44 J. Cui, A. P. Beyler, I. Coropceanu, L. Cleary, T. R. Avila, Y. Chen, J. M. Cordero, S. L. Heathcote, D. K. Harris and O. Chen, Evolution of the single-nanocrystal photoluminescence linewidth with size and shell: implications for exciton–phonon coupling and the optimization of spectral linewidths, *Nano Lett.*, 2016, **16**, 289–296.

45 S. Wang, Y. Xie, W. Jiang, B. Liu, K. Shi and K. Pan, Incorporation sodium ions into monodisperse lead-free double perovskite $Cs_2AgBiCl_6$ nanocrystals to improve optical properties, *Chin. Chem. Lett.*, 2024, **35**, 108521.

46 L. Zhou, J. F. Liao, Y. Qin, X. D. Wang, J. H. Wei, M. Li, D. B. Kuang and R. He, Activation of self-trapped emission in stable bismuth-halide perovskite by suppressing strong exciton-phonon coupling, *Adv. Funct. Mater.*, 2021, **31**, 2102654.

47 M. Ledinsky, T. Schönfeldová, J. Holovský, E. Aydin, Z. k. Hájková, L. Landová, N. Neyková, A. Fejfar and S. De Wolf, Temperature dependence of the urbach energy in lead iodide perovskites, *J. Phys. Chem. Lett.*, 2019, **10**, 1368–1373.

48 B. Subedi, C. Li, C. Chen, D. Liu, M. M. Junda, Z. Song, Y. Yan and N. J. Podraza, Urbach energy and open-circuit

voltage deficit for mixed anion–cation perovskite solar cells, *ACS Appl. Mater. Interfaces*, 2022, **14**, 7796–7804.

49 B. Slimi, M. Mollar, I. Ben Assaker, A. Kriaa, R. Chtourou and B. Marí, Synthesis and characterization of perovskite $FAPbBr_{3-x}I_x$ thin films for solar cells, *Monatsh. Chem. – Chem. Mon.*, 2017, **148**, 835–844.

50 H. Wang, Z. Chen, F. Tian, G. Zheng, H. Wang, T. Zhang, J. Qin, X. Gao, P. A. van Aken and L. Zhang, Impacts of the lattice strain on perovskite light-emitting diodes, *Adv. Energy Mater.*, 2023, **13**, 2202185.

51 F. Zhang, B. Yang, K. Zheng, S. Yang, Y. Li, W. Deng and R. He, Formamidinium lead bromide ($FAPbBr_3$) perovskite microcrystals for sensitive and fast photodetectors, *Nano-Micro Lett.*, 2018, **10**, 1–8.

52 C. Ma, M. F. Lo and C. S. Lee, Stabilization of organometallic halide perovskite nanocrystals in aqueous solutions and their applications in copper ion detection, *Chem. Commun.*, 2018, **54**, 5784–5787.

53 R. Kumar, J. Kumar, P. Srivastava, D. Moghe, D. Kabra and M. Bag, Unveiling the morphology effect on the negative capacitance and large ideality factor in perovskite light-emitting diodes, *ACS Appl. Mater. Interfaces*, 2020, **12**, 34265–34273.

54 X. Xiao, T. Ye, J. Sun, X. Qu, Z. Ren, D. Wu, S. Ding, X. W. Sun, W. C. H. Choy and K. Wang, Capacitance–voltage characteristics of perovskite light-emitting diodes: Modeling and implementing on the analysis of carrier behaviors, *Appl. Phys. Lett.*, 2022, **120**, 24.

55 P. Pahner, H. Kleemann, L. Burtone, M. L. Tietze, J. Fischer, K. Leo and B. Lüssem, Pentacene Schottky diodes studied by impedance spectroscopy: Doping properties and trap response, *Phys. Rev. B: Condens. Matter Mater. Phys.*, 2013, **88**, 195205.

56 X. Peng, X. Yang, D. Liu, T. Zhang, Y. Yang, C. Qin, F. Wang, L. Chen and S. Li, Targeted distribution of passivator for polycrystalline perovskite light-emitting diodes with high efficiency, *ACS Energy Lett.*, 2021, **6**, 4187–4194.

57 X. Xiao, K. Wang, T. Ye, R. Cai, Z. Ren, D. Wu, X. Qu, J. Sun, S. Ding and X. W. Sun, Enhanced hole injection assisted by electric dipoles for efficient perovskite light-emitting diodes, *Commun. Mater.*, 2020, **1**, 81.

58 Y. Chen, C. Yan, Z. Chen, X. Zeng, Q. Wang, S. Yang, L. Pan, C. Li, M. Mu and W. Li, Interfacial Coulomb-enhanced charge injection for efficient perovskite light-emitting diodes, *Mater. Today Phys.*, 2024, 101413.

59 R. Kötz and M. Carlen, Principles and applications of electrochemical capacitors, *Electrochim. Acta*, 2000, **45**, 2483–2498.

60 Y. Liu, M. Bag, L. A. Renna, Z. A. Page, P. Kim, T. Emrick, D. Venkataraman and T. P. Russell, Understanding interface engineering for high-performance fullerene/perovskite planar heterojunction solar cells, *Adv. Energy Mater.*, 2016, **6**, 1501606.

61 C. Bi, Z. Yao, X. Sun, X. Wei, J. Wang and J. Tian, Perovskite quantum dots with ultralow trap density by acid etching–driven ligand exchange for high luminance and stable pure-blue light-emitting diodes, *Adv. Mater.*, 2021, **33**, 2006722.

62 Y. Jia, H. Yu, Y. Zhou, N. Li, Y. Guo, F. Xie, Z. Qin, X. Lu and N. Zhao, Excess ion-induced efficiency roll-off in high-efficiency perovskite light-emitting diodes, *ACS Appl. Mater. Interfaces*, 2021, **13**, 28546–28554.

63 H. Kim, L. Zhao, J. S. Price, A. J. Grede, K. Roh, A. N. Brigeman, M. Lopez, B. P. Rand and N. C. Giebink, Hybrid perovskite light emitting diodes under intense electrical excitation, *Nat. Commun.*, 2018, **9**, 4893.

64 Z. Li, Z. Chen, Y. Yang, Q. Xue, H. L. Yip and Y. Cao, Modulation of recombination zone position for quasi-two-dimensional blue perovskite light-emitting diodes with efficiency exceeding 5%, *Nat. Commun.*, 2019, **10**, 1027.

65 Y. Shi, W. Wu, H. Dong, G. Li, K. Xi, G. Divitini, C. Ran, F. Yuan, M. Zhang and B. Jiao, A strategy for architecture design of crystalline perovskite light-emitting diodes with high performance, *Adv. Mater.*, 2018, **30**, 1800251.

66 H. Wang, Z. Chen, J. Hu, H. Yu, C. Kuang, J. Qin, X. Liu, Y. Lu, M. Fahlman and L. Hou, Dynamic redistribution of mobile ions in perovskite light–emitting diodes, *Adv. Funct. Mater.*, 2021, **31**, 2007596.